Int J Adv Manuf Technol (2015) 78:723–736
DOI 10.1007/s00170-014-6674-x

ORIGINAL ARTICLE

A numerical approach to modeling keyhole laser welding

Georgios Pastras · Apostolos Fysikopoulos · Christos Giannoulis · George Chryssolouris

Received: 23 June 2014 / Accepted: 1 December 2014 / Published online: 13 December 2014

Abstract A numerical study of the laser welding process is presented. The numerical model is based on a combination of the enthalpy method and the finite difference techniques applied to the heat equation that can bypass the manual enforcement of the jump condition at the phase-separating surfaces. Minimal application of the "life and death of elements techniques" is required in order for the dynamics of the keyhole to be captured. This analysis results in the construction of the flowchart of a time-stepping algorithm, suitable for any software platform or computer language.

Keywords Laser welding · Process modeling · Enthalpy method · Finite difference

1 Introduction

For several decades, laser processing has been an increasingly indispensable part of competitive manufacturing throughout the world [1, 2]. Laser cutting has recently reached a certain level of maturity [3, 4]. Process variable data are available for a range of materials, based, however, mainly on experimental process maps. Laser welding (LW) has also evolved significantly. Laser welding is used when it is essential that the size of the heat-affected zone (HAZ) be limited, to reduce the roughness of the welded surface and to eliminate mechanical effects [5, 6].

In the last few years, a new laser process, the remote laser welding (RLW) has emerged. RLW [7] has been developed and implemented to improve the productivity and flexibility of conventional laser welding. In principle, RLW is based on a scanner that assists in the deflection and positioning of the laser beam onto the workpiece surface allowing high travelling speed [8, 9]. Currently, it is mainly applied to mass production automotive assembly lines on which a high number of welding seams are being processed [10–13]. A number of RLW systems are used for a wide range of automotive applications such as closures, pillars, and seats [14, 15].

Modeling of the laser welding process can assist in better comprehending in the way that parameters affect the process, in order to reduce experimental costs, optimize production, assist monitoring and provide easy and fast answers to "what if" scenarios. A number of studies have been carried out attempting to model different welding states and various configurations, such as lap or butt welding, using either analytical, semi-empirical, or empirical methods.

In this paper, a numerical approach to modeling keyhole laser welding, considering heating, melting, and evaporation phases by using the enthalpy method and finite differences at the same time, will be presented. The shape of the keyhole is introduced in the model using life and death of elements techniques. The paper is structured into six main sections. The second section is an extensive literature review of LW modeling. In the third section, the modeling approach is described in detail, while in the forth, the implementation of the model into a software tool is presented. Finally, conclusions and directions for future extensions are summarized in the fifth and sixth sections.

2 Literature review

2.1 LW modeling

The two fundamental classes of laser welding are those of conduction and keyhole or penetration welding. The transition

G. Pastras (✉) · A. Fysikopoulos · C. Giannoulis · G. Chryssolouris
Laboratory for Manufacturing Systems and Automation, Department of Mechanical Engineering and Aeronautics, University of Patras, 26500 Patras, Greece
e-mail: xrisol@mech.upatras.gr

from conduction welding to keyhole depends on the peak laser intensity and duration of the laser pulse applied to the workpiece. When the heat transfer phenomena (conduction, convection, and radiation) take place (Fig. 1), they are usually accompanied by the buildup of the capillary of ionized metal vapor (mainly in keyhole welding) that can be observed when the intensity of the laser beam is higher than 10^6 W/cm^2 [16].

In general, the modeling problem of keyhole laser welding is considered as a three-phase moving boundary problem with two moving interfaces: solid to liquid interface and liquid to vapor interface [17]. The literature review shows that numerous models have been developed in order for a wide range of conditions to be studied. Several models try to reduce the calculation effort to acquire fast results by simplifying the problem and, at the same time, to capture the key features of the process in order to provide a good insight [18, 19]. However, these simplifications lead to the loss of important information and, consequently, to wrong decisions or to a model that is neither general nor widely applicable.

The incorporation of the vapor phase (keyhole) makes the problem more complex [20]. By using the correct assumptions, its accuracy can be succeeded numerically [21–28, 30] and even analytically [16, 29]. Several researchers have employed the finite element method (FEM); nevertheless, these methods need both increased computational effort and the model calibration with experimental data. Fewer studies are found to be related to the welding of dissimilar materials, which indicate increased complexity in terms of modeling [19, 30].

Multiple reflections of the laser beam on the keyhole cavity surface are a crucial part of modeling that needs to be considered in order for higher accuracy that will increase again the modeling complexity to be achieved [31]. The principal mechanism of energy absorption in keyhole welding is the Fresnel absorption, which is strongly affected when multiple reflections of the beam on the keyhole are present [20, 32].

2.2 RLW implications

The basic principles of modeling for RLW are the same, although there are few published studies on this topic, thus limiting the knowledge of any implications that may arise. Tsoukantas et al. [7] presented an experimental approach for RLW, investigating the behavior of the lap-welded geometrical characteristics with respect to the laser beam inclination. The type of laser, the beam spot diameter, and the beam inclination have a significant effect on the behavior of the welds' dimensions as incidence varies.

In the automotive industry, galvanized steels are widely used for the body in white production [30]. A major problem in the application of LW to this kind of materials is that zinc is prone to evaporate during welding process due to its relatively low boiling point (906 °C) as compared to the melting temperature of steel (1530 °C). Thus, a suitable gap has to be maintained during the process in overlap configurations, in order to prevent the pressurization of the vaporized zinc until it meets the keyhole. This phenomenon may damage the weld zone and generate porosity in the seam, resulting in poor surface quality, reduced strength, and inferior quality resistance. If the joint gap is small, it is unfavorable for the escape of zinc vapors and the welding process turns out to be unstable and has bad weld appearance [33–35]. On the other hand, if the joint gap is oversized or the incident angle exceeds a critical value [36], it will be impossible for the two parts to be mutually melted.

When a gap between the two plates exists, there is some difference in the process thermodynamics. The gap is functioning as a thermal insulator, not allowing

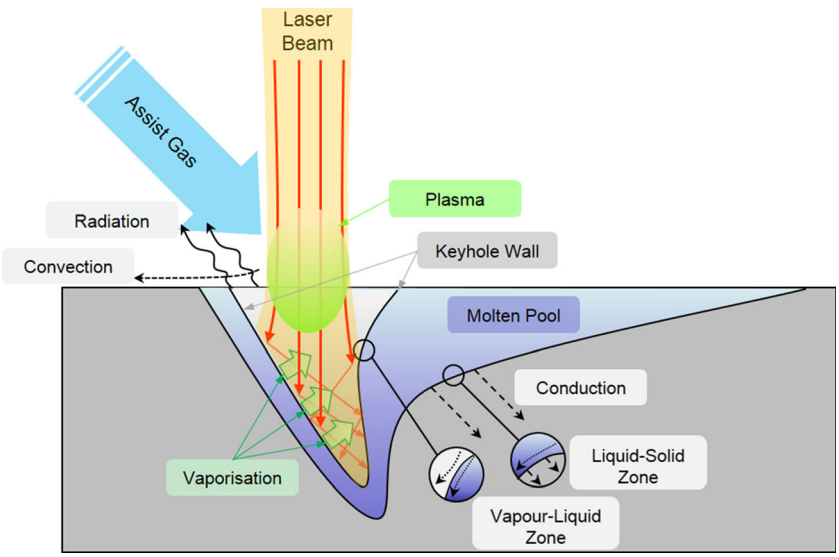

Fig. 1 The thermal phenomena in the welding process

the diffusion of heat from the top laminate to the bottom before the gap is filled with melt material. Moreover, the existence of the gap complicates the material flow during the process. The above renders the modeling of RLW process even more complicated and the relevant literature very limited.

3 Keyhole welding modeling

3.1 Simplifying assumptions

During the LW process, a large number of physical phenomena simultaneously take place; thus, some simplifying assumptions have to be made in any modeling approach:

1. Evaporated material is assumed to be instantly removed from the workpiece; i.e., the absorption of the laser beam by the material vapors is considered negligible.
2. Alterations in the effective absorptivity of the workpiece material due to multiple reflections on the keyhole walls are considered negligible.
3. Since this study focuses on the welding of metals, which are heat conductors, the heat transfer through convection and radiation is negligible in comparison to the heat transfer due to conduction.
4. Material thermal properties are considered being independent of the temperature.
5. Typically, the laser head is scanning the surface of the workpiece with speed v, creating a stitch-shaped rather than a spot-shaped weld. As a result, at any point in the center of the stitch, the laser beam has been acting for a time interval equal to $t=2r/v$, where r is the spot radius. Instead of following a three-dimensional approach, the process is regarded two-dimensional. It is considered that the laser head is stationary and the laser beam is on for a time interval equal to t.

3.2 The problem setup

The simplifying assumptions of Sect. 3.1 have been made on the basis that the dominant phenomena during the LW process are the heat conduction, the melting and evaporation phase transitions, the laser beam defocusing, and the evolution of the workpiece surface due to the formation of the keyhole.

3.2.1 The laser power density

It is assumed that the laser source is functioning in continuous mode. When a keyhole is formed, the laser beam hits the workpiece in a position deeper than the initial workpiece surface, thus rendering defocusing important. The radius of the spot as function of the depth is given by [37]

$$r_b(z) = r_0\sqrt{1+\left(M^2\frac{\lambda(z-\delta f)}{\pi {r_0}^2}\right)^2}, \tag{3.1}$$

where M is the beam quality parameter, λ is the laser wavelength, and δf is the z coordinate of the focal plane.

A Gaussian profile is assumed for the laser beam intensity (TEM00). Thus, the laser beam intensity as a function of the distance from the laser beam axis r and the depth z is described by

$$I(r,z) = I_0\frac{{r_0}^2}{{r_b(z)}^2}e^{-2\frac{r^2}{{r_b(z)}^2}}. \tag{3.2}$$

I_0 is the intensity of the laser beam at the beam axis and at the focal level. It is specified by the laser power P and the spot radius r_0 as

$$I_0 = \frac{2P}{\pi {r_0}^2}. \tag{3.3}$$

In later considerations, it should be useful to specify the angle of the laser beam with the vertical axis. This is given by

$$\theta_l(r,z) = \arctan\frac{r(z-\delta f)\left(M^2\frac{\lambda}{\pi {r_0}^2}\right)^2}{1+\left(M^2\frac{\lambda(z-\delta f)}{\pi {r_0}^2}\right)^2}. \tag{3.4}$$

3.2.2 Heating phase

The rotational symmetry of the problem allows for the study of the process to be made in two spatial dimensions, since the symmetry enforces the problem solution to be independent from the angle measured from the laser beam axis. The following formulation of the problem, as well as the numerical modeling, is developed under this scope; thus, the angular coordinate will be disregarded from now on.

In order to study the heating of the workpiece surface, it is required that the heat equation be solved with the appropriate initial and boundary conditions so as for the temperature field to be found. The heat equation is

$$\nabla^2 T(t,r,z) = \frac{1}{a}\frac{\partial T(t,r,z)}{\partial t}, \tag{3.5}$$

where a is the material's thermal diffusivity. Thermal diffusivity is a function of temperature in general; however, it will be considered constant for the simplicity of the results.

The appropriate initial condition is

$$T(0,r,z) = T_0, \tag{3.6}$$

where T_0 is the environment temperature.

The boundary conditions for the heat equation are defined by the heat flux because of the laser beam. Since during the heating phase, there is no keyhole formed, the laser intensity should be considered at $z=0$.

$$\left.\frac{\partial T(t,r,z)}{\partial z}\right|_{z=0} = -\frac{1}{k}(1-R)I(r,0), \tag{3.7}$$

where k is the material's thermal conductivity and R is its reflectivity.

3.2.3 Melting phase

When the surface temperature reaches the melting point, the two phases of the material, solid and liquid, coexist and interchange heat. In both regions, the heat equation is satisfied

$$\nabla^2 T_s(t,r,z) = \frac{1}{a_s}\frac{\partial T_s(t,r,z)}{\partial t}, \tag{3.8}$$

$$\nabla^2 T_l(t,r,z) = \frac{1}{a_l}\frac{\partial T_l(t,r,z)}{\partial t}, \tag{3.9}$$

where the index l stands for liquid and the index s stands for solid.

The two regions are separated by a surface at $\vec{r}_{ls} = \vec{S}_{ls}(t,r) = R_{ls}(t,r)\hat{e}_r + Z_{ls}(t,r)\hat{e}_z$. The temperature on the phase separating surface equals the melting temperature T_m

$$T_l(t,R_{ls}(t,r),Z_{ls}(t,r)) = T_s(t,R_{ls}(t,r),Z_{ls}(t,r)) = T_\mathrm{m}. \tag{3.10}$$

The velocity of the moving boundary between the two regions is set by the latent heat of fusion L_f. The relevant boundary condition is the so-called Stefan condition, and it is actually energy conservation concerning the latent heat of fusion.

$$-k_l \vec{\nabla} T_l(t,r,z)\Big|_{\vec{r}=\vec{S}_{ls(t,r)^-}} + k_s \vec{\nabla} T_s(t,r,z)\Big|_{\vec{r}=\vec{S}_{ls(t,r)^+}} = L_f \rho \frac{d\vec{S}_{ls}(t,r)}{dt}. \tag{3.11}$$

As there is no erosion front, the volume of the material remains approximately constant and the laser always hits the initial surface of the workpiece making laser defocusing irrelevant. Thus, the boundary condition (3.7) is still valid for the melting phase.

3.2.4 Evaporation phase

Finally, when the surface reaches the evaporation temperature, it gives rise to the keyhole formation. Similarly to the melting phase, another Stefan condition, concerning the gas-liquid phase separating surface, has to be included. However, a significant difference is the presence of the gaseous state, which when formed, it escapes altering the geometry of the workpiece and preventing the description of this region with the heat equation. As a result, the problem is divided into three regions, but only in two of those, the heat equation is valid, as described by Eqs. (3.8) and (3.9). The boundary between the liquid and the gaseous state is described similarly to the solid-liquid boundary as a surface $\vec{r}_{gl} = \vec{S}_{gl}(t,r) = R_{gl}(t,r)\hat{e}_r + Z_{gl}(t,r)\hat{e}_z$. The temperature in the liquid region follows

$$T_l\big(t,R_{gl}(t,r),Z_{gl}(t,r)\big) = T_v, \tag{3.12}$$

as a result of continuity. Finally, the relevant Stefan condition has to be expressed differently, since there is no heat equation in the gaseous region. On the contrary, the heat current is directly described by the absorbed laser power density. Given that the keyhole is present, both the incoming heat current has to be taken perpendicularly to the gas-liquid phase separating surface and the absorbed intensity has to be calculated carefully, since the laser beam is not perpendicular to the workpiece surface because of the keyhole

$$(1-R)I\big(R_{gl}(t,r),Z_{gl}(t,r)\big)\cos(\theta_{gl}-\theta_l)\hat{e}_{gl} + k_l \vec{\nabla} T_l(t,r,z)\Big|_{\vec{r}=\vec{S}_{gl(t,r)^+}} = L_v \rho \frac{d\vec{S}_{gl}(t,r)}{dt}, \tag{3.13}$$

where $\hat{e}_{gl}$ is the inward perpendicular surface to the gas-liquid phase separating surface. θ_{gl} and θ_l are the angle of the boundary surface and the angle of the laser beam with the vertical axis, respectively. This condition also substitutes the boundary condition (3.7) during the evaporation phase.

3.3 The numerical model

The problem without further simplifying assumptions has to be approximated with a numerical method.

3.3.1 The enthalpy method

A finite difference approach can be applied to express a discrete version of the heat equation as a set of difference equations. Since the heat equation is first order in time, these equations can be easily solved, time slice by time slice. However, such an approach has the disadvantage of having the phase transitions dealt manually, as described by Eqs. (3.11) and (3.13). Additionally, the heat equation has to be solved separately in the region of the solid and liquid phases. The above problem requires more ingredients from the finite element techniques, specifically, the characterization of each node by a phase index and the "life and death of elements" techniques for the nodes that change phase. Such front tracking approaches work well for simple Stefan problems [38]; however, in more realistic problems, complications

such as multiple fronts, disappearing phases, and nonpredictable behavior may appear, even in one-dimensional cases. Moreover, if the governing equations are based on the Stefan formulation, in the region of the phase change, the moving boundary conditions have to be accounted for, and thus, the application of a fixed grid numerical solution is ruled out, as deforming grids are required to account for the time-dependent positions of the phase separating fronts.

For the above reason, front tracking methods are not viable for the modeling of realistic processes that involve phase changes. The enthalpy method can be adopted (see e.g., [39, 40]). The nonsmoothness of the temperature field at a phase separating surface is due to the fact that during a phase transition, the incoming heat does not correspond to an increase of temperature, because of the latent heat. This phenomenon can be dealt more easily by introducing a new field corresponding to the enthalpy density. Then, the second derivative of the temperature will result in a rate of change for the enthalpy density while the enthalpy density will be connected to the local temperature, taking into account not only the specific heat, but also the latent heat of fusion and evaporation. After that, the jump condition (Stefan condition) is not manually enforced on the solution, but it is automatically obeyed, as a "natural boundary condition" in the sense of the calculus of variations. This means that the heat equation, including phase transitions, can be expressed as a set of two equations

$$\frac{\partial U}{\partial t} = k\nabla^2 T, \tag{3.14}$$

$$T = T(U), \tag{3.15}$$

where enthalpy density and temperature are connected through

$$T(U) = \begin{cases} \dfrac{U}{\rho c}, & U < \rho c T_{\mathrm{m}}, \\ T_{\mathrm{m}}, & \rho c T_{\mathrm{m}} < U < U_{\mathrm{m}}, \\ \dfrac{U - \rho L_f}{\rho c}, & U_{\mathrm{m}} < U < \rho\left(cT_v + L_f\right), \\ T_v, & \rho\left(cT_v + L_f\right) < U < U_{\mathrm{v}}, \end{cases} \tag{3.16}$$

where U_{m} and U_{v} are the required enthalpy densities for the melting and vaporization phase transition, respectively. They are equal to

$$U_{\mathrm{m}} = \rho\left(cT_{\mathrm{m}} + L_f\right), \tag{3.17}$$

$$U_{\mathrm{v}} = \rho\left(cT_v + L_f + L_v\right). \tag{3.18}$$

The relation between enthalpy density and temperature is indicated in Fig. 2.

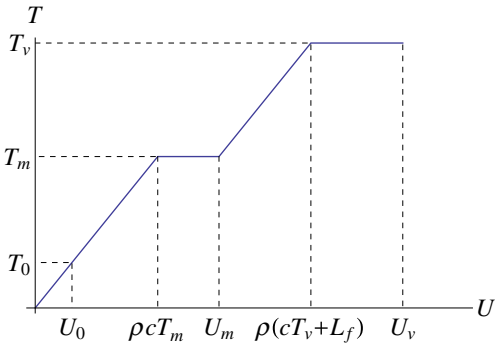

Fig. 2 Relation between enthalpy density and temperature

3.3.2 A finite difference approach

The enthalpy method can be applied to both a finite difference [41, 42] and a finite element numerical algorithm [43, 44]. It would be desirable to use the strictest possible formulation of the problem, namely the finite difference method, as such an approach combined with the enthalpy method is proven to provide accurate numerical solutions [45, 46]. Moreover, the finite differences are preferable, since they require easier user input than the finite elements do, and moreover, the problem of approximating an initial solution such as in the Galerkin method is bypassed. The latter can be an important problem, as the solution has to be nonsmooth due to the phase changes increasing the difficulty of specifying a close enough initial solution.

Although the enthalpy method bypasses the manual enforcement of the jump conditions for the two phase transitions that take place during the laser welding process, special care has to be taken for the gaseous state. Nodes that turn to the gaseous state have to be removed from the lattice with severe consequences for the formulation of the problem, such as the laser beam passing freely through these nodes and the angle between the laser beam and the workpiece surface and, thus, the in-falling energy density being altered. As a result, the proposed method has to adopt some life and death of elements techniques.

In this study, the discrete times are considered uniformly spaced in the interval $0 \le t \le t_{\max}$, where $t_{\max}$ is the maximum time considered. There are nodes at $t=0$ and $t=t_{\max}$, thus $t_i=(i-1)\Delta t$, where i takes values from 1 to N_t and $\Delta t=t_{\max}/(N_t-1)$. Similarly, the discrete radii and depths are also considered uniformly spaced, thus $r_j=(j-1)\Delta r$, where j takes values from 1 to N_r and $\Delta r=R/(N_r-1)$ and $z_k=(k-1)\Delta z$, where k takes values from 1 to N_z and $\Delta z=Z/(N_z-1)$. The temperature field is a finite set of the elements $T_{ijk}=T(t_i,r_j,z_k)$. For the clarity of the description, from now on, the indexes i, j, and k will always refer to the discretized time coordinate, distance from the beam axis, and depth, respectively.

The discrete version of the set of Eqs. (3.14) and (3.15), for the implemented finite difference modeling of laser welding, is

$$\frac{U_{i+1,j,k}-U_{i,j,k}}{\Delta t}=k\left(\frac{T_{i,j+1,k}-2T_{i,j,k}+T_{i,j-1,k}}{\Delta r^2}+\frac{1}{r_j}\frac{T_{i,j+1,k}-T_{i,j,k}}{\Delta r}+\frac{T_{i,j,k+1}-2T_{i,j,k}+T_{i,j,k-1}}{\Delta z^2}\right), \tag{3.19}$$

$$T_{ijk}=T\left(U_{ijk}\right), \tag{3.20}$$

The initial conditions U_{1jk} and T_{1jk} are given in the form of the initial conditions

$$T_{1jk}=T_0, \tag{3.21}$$

$$U_{1jk}=\rho cT_0\equiv U_0, \tag{3.22}$$

since the material initially is in the solid phase.

It is clear from the Eqs. (3.19) and (3.20) that the problem can be integrated time slice by time slice. The Eq. (3.19) allows the calculation of the enthalpy density values in the next time step, which can be translated into the temperatures of the next time step using Eq. (3.20) and so on.

3.3.3 Specification of the keyhole shape

When the evaporation starts, the boundary of the nonevaporated region has to be specified. This is a fact that has to be necessarily dealt with the life and death of elements techniques. In every vertical line, the boundary can be specified as the uppermost element of the lattice that has enthalpy density smaller than the critical [46].

$$bz_{ij}=\min\left\{k\middle|U_{ijk}<U_{\mathrm{v}}\right\}. \tag{3.23}$$

All elements in the (i,j) vertical column, characterized by $k<bz_{ij}$, are in this language considered as "dead."

However, as shown in Fig. 3, scanning only along the z directions is not going to provide all points of the boundary, and the latter is required for the specification of the laser beam's angle of incidence and specifically, when the boundary conditions, related to radial derivatives, are applied. Thus, it is necessary to scan along the horizontal directions, too

$$br_{ik}=\min\left\{j\middle|U_{ijk}<U_{\mathrm{v}}\right\}. \tag{3.24}$$

Once the boundaries have been determined, the angle of the keyhole surface to the vertical direction has to be specified. The central difference approximation of the derivative can be used everywhere except for the first and the last points of the lattice, where the advanced and the retarded definitions have to be used, respectively,

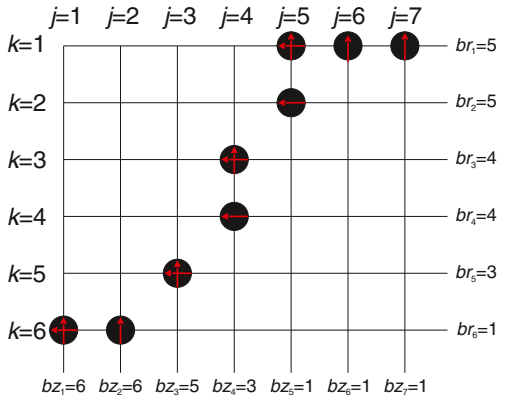

Fig. 3 Specification of the boundary. The *red arrows* indicate the direction that can specify a given boundary element; all elements are specified through scanning of at least one direction

$$\theta z_{ij}=\arctan\left[\left(bz_{i,j-1}-bz_{i,j+1}\right)\frac{\Delta z}{2\Delta r}\right], \tag{3.25}$$

$$\theta z_{i1}=\arctan\left[\left(bz_{i,1}-bz_{i,2}\right)\frac{\Delta z}{\Delta r}\right], \tag{3.26}$$

$$\theta z_{i,N_r}=\arctan\left[\left(bz_{i,N_r-1}-bz_{i,N_r}\right)\frac{\Delta z}{\Delta r}\right], \tag{3.27}$$

$$\theta r_{ik}=\operatorname{arccot}\left[\left(br_{i,k-1}-br_{i,k+1}\right)\frac{\Delta r}{2\Delta z}\right], \tag{3.28}$$

$$\theta r_{i1}=\operatorname{arccot}\left[\left(br_{i,1}-br_{i,2}\right)\frac{\Delta r}{\Delta z}\right], \tag{3.29}$$

$$\theta r_{i,N_z}=\operatorname{arccot}\left[\left(br_{i,N_z-1}-br_{i,N_z}\right)\frac{\Delta r}{\Delta z}\right]. \tag{3.30}$$

As expected, the angles θr and θz are equal when they refer to the same point. However, since bz or br alone cannot cover the entire boundary, both angles have to be determined.

It has to be noticed that the workpiece surface is not perpendicular to the laser beam, due to both angles of the boundary and the laser beam defocusing, as described by Eq. (3.4). This means that the incident intensity is smaller than it was initially calculated, as it is spread to a larger area. Specifically, the absorbed power density, at a given point of the boundary, is equal to

$$PD_{ij}=(1-R)I\left(r_j,z_{bz_{ij}}\right)\cos\left[\theta z_{ij}-\theta_l\left(r_j,z_{bz_{ij}}\right)\right], \tag{3.31}$$

if a boundary of a vertical slice is considered, and

$$PD_{ik} = (1-R)I(r_{br_{ik}}, z_k)\cos[\theta r_{ik} - \theta_l(r_{br_{ik}}, z_k)], \tag{3.32}$$

if a boundary of a horizontal slice is considered.

As long as the boundary conditions are considered, the aforementioned power densities set the magnitude of the temperature gradient at the boundary. The direction of the temperature gradient is set by the direction of the boundary surface. Thus, the partial derivatives at the boundary are equal to

$$\left.\frac{dT}{dz}\right|_{i,j,bz_{ij}} = -\frac{PD_{ij}}{k}\cos\theta z_{ij}, \tag{3.33}$$

if a boundary of a vertical slice is considered, and

$$\left.\frac{dT}{dr}\right|_{i,br_{ik},k} = -\frac{PD_{ik}}{k}\sin\theta r_{ik}, \tag{3.34}$$

if a boundary of a horizontal slice is considered.

3.3.4 The boundary conditions

Finally, the definition of the second spatial derivatives is problematic at $j=br_{ik}$, $j=N_r$, $k=bz_{ij}$, and $k=N_z$, since it involves an element of the lattice that is absent. All of these positions correspond to the physical boundaries of the problem except for the case $j=br_{ik}$ when $br_{ik}=1$, which corresponds to the beam axis, where the Laplacian expressed in polar coordinates is singular. The boundary condition, described by Eq. (3.7) and a similar one for the opposite boundary describing the vanishing heat flow, can be expressed as

$$\frac{T_{i,j,k+1} - 2T_{i,j,k} + T_{i,j,k-1}}{\Delta z^2} \overset{k=bz_{ij}}{\rightarrow} \frac{T_{i,j,bz_{ij}+1} - T_{i,j,bz_{ij}}}{\Delta z^2} + \frac{1}{\Delta z}\frac{PD_{ij}}{k}\cos\theta z_{ij}, \tag{3.35}$$

$$\frac{T_{i,j,k+1} - 2T_{i,j,k} + T_{i,j,k-1}}{\Delta z^2} \overset{k=N_z}{\rightarrow} -\frac{T_{i,j,N_z} - T_{i,j,N_z-1}}{\Delta z^2}, \tag{3.36}$$

$$\frac{T_{i,j+1,k} - 2T_{i,j,k} + T_{i,j-1,k}}{\Delta r^2} + \frac{1}{r_j}\frac{T_{i,j+1,k} - T_{i,j,k}}{\Delta r} \overset{j=br_{ik}}{\rightarrow} \frac{T_{i,br_{ik}+1,k} - T_{i,br_{ik},k}}{\Delta r^2} + \frac{1}{\Delta r}\left(1 - \frac{1}{r_{br_{ik}}}\right)\frac{PD_{ik}}{k}\sin\theta r_{ik}, \tag{3.37}$$

$$\frac{T_{i,j+1,k} - 2T_{i,j,k} + T_{i,j-1,k}}{\Delta r^2} + \frac{1}{r_j}\frac{T_{i,j+1,k} - T_{i,j,k}}{\Delta r} \overset{j=N_r}{\rightarrow} -\frac{T_{i,N_r,k} - T_{i,N_r-1,k}}{\Delta r^2}, \tag{3.38}$$

where PD_{ik} and PD_{ik} are given by Eqs. (3.31) and (3.32). For the $r=0$ singularity, the solution is provided by the fact that due to the symmetry of the problem, the temperature has to be stationary at the z-axis in every horizontal plane. This means that the temperature field in the region close to the $r=0$ axis can be expressed as

$$T(t,r,z) \simeq c_0(t,z) + c_2(t,z)r^2 + \ldots, \tag{3.39}$$

meaning that the terms $\frac{\partial^2 T}{\partial r^2}$ and $\frac{1}{r}\frac{\partial T}{\partial r}$ become equal at the $r=0$ axis. Thus, the appropriate boundary condition at $j=1$ is

$$\frac{T_{i,j+1,k} - 2T_{i,j,k} + T_{i,j-1,k}}{\Delta r^2} + \frac{1}{r_j}\frac{T_{i,j+1,k} - T_{i,j,k}}{\Delta r} \overset{j=1}{\rightarrow} 2\frac{T_{i,2,k} - T_{i,1,k}}{\Delta r^2}. \tag{3.40}$$

The problem is completely described by Eqs. (3.19) and (3.20) and the boundary conditions (3.35), (3.36), (3.38), and (3.40), which can be integrated time slice by time slice, providing the temperature field as a function of depth and time.

3.3.5 Generalization of the model for temperature-dependent material properties

In the model presented above, the material properties are considered independent of the temperature. However, the material density, thermal conductivity, and specific heat are actually temperature functions. The model can be easily extended taking into consideration the temperature dependence of these quantities.

The most important adjustment to be made is the modification of the relation between temperature and enthalpy density (3.16), which is used in the finite difference method in (3.20). This relation is now given by

$$U(T) = U(T_0) + \int_{T_0}^{T} \rho(T)c(T)dt. \tag{3.41}$$

Equation (3.16) should be substituted with the inverse function of (3.41). Note that the specific heat has singularities at the temperatures of the phase transitions; however, the integral (3.41) always converges. Moreover, since the specific heat is always positive, the enthalpy is an increasing function of temperature; thus, it is invertible.

The study made in the above sections can be taken as the special case, where the material density is taken to be constant and the specific heat is considered being equal to

$$c(T) = c + L_f\delta(T - T_m) + L_v\delta(T - T_v), \tag{3.42}$$

where $\delta(T)$ is Dirac's delta function. Then, the inverse of (3.41) is given by Eq. (3.16).

Finally, the material's thermal conductivity has to be considered as a function of the temperature, meaning that k in Eq. (3.19) has to be substituted with $k(T_{i,j,k})$ and k in Eqs. (3.33) and (3.34) has to be substituted with $k(T_v)$.

Table 1 The material thermal properties used for the graphs exposing the outcome of the model

T_0	300 K
T_m	1680 K
T_v	2861 K
k	66 W/m K
α	16.4×10^{-6} m^2/s
R	0.8
ρ	7775 kg/m^3
L_f	200 kJ/kg
L_v	6090 kJ/kg

3.4 The solution of the numerical model

A simple example based on the model build in Sect. 2.2 has been considered. For this example, the material properties given in Table 1, the laser properties in Table 2, and the lattice variables in Table 3 have been used. The material properties used are typical thermal properties of mild steels, and the laser properties are typical values of CO_2 laser sources. The laser variables correspond to t_{max}=8 msec, which is the value used for the lattice properties.

The outcome of the model for several different time instants is shown in Figs. 4, 5, 6, 7, and 8. In these figures, the development of the keyhole can be understood as a function of time. It should be noticed that the volume of the melted pool is larger than it is shown in the figures, since the elements being further from the laser beam axis correspond to larger volumes. Specifically, the element with indexes (j,k) corresponds to volume equal to

$$\Delta V_{jk} = 2\pi j \Delta r \Delta z. \tag{3.43}$$

It is necessary that an extended comparison of the model's outcome with experimental results be performed. Such study is going to be presented in future work. However, a comparison of the model's outcome with experiments found in literature [20] is depicted in Fig. 9, in order to check that the model predicts correctly the order of magnitude of the weld depth and the form of its dependence on process variables, namely the welding speed. Figure 9 suggests that the model makes a close reproduction of the experimental results.

Table 2 The laser variables used for the graphs exposing the outcome of the model

r_0	0.25 mm
δf	0
M	1.3
λ	10.6 μm
P	4.0 kW
v	2.0 m/min

Table 3 The lattice variables used for the graphs exposing the outcome of the model

z_{max}	2 mm
N_z	100
r_{max}	1 mm
N_r	50
t_{max}	15 msec
N_t	3000

4 Model implementation

The main implementation procedure is described in Fig. 10. An important detail, before reaching the main calculation subroutines, is a basic check of the lattice properties defined by the user. It can be proven that the finite difference method for the heat equation cannot be numerically stable unless $a\Delta t/\Delta z^2<1/2$ and $a\Delta t/\Delta r^2<1/4$. If these conditions are not satisfied, then the temperature evolution with time will appear to be oscillatory with exponentially increasing amplitude. If the choice of the lattice variables is not appropriate, the user has to render them.

The most important part of the algorithm is the "calculate the temperature field" subroutine. The appropriate information about this subroutine is analyzed in Sect. 3.3. As the different boundary conditions affect different parts of the two-dimensional Laplacian, in the following, the radial and vertical parts of the Laplacian are defined separately as

$$L_r \equiv \frac{T_{i,j+1,k} - 2T_{i,j,k} + T_{i,j-1,k}}{\Delta r^2} + \frac{1}{r_j}\frac{T_{i,j+1,k} - T_{i,j,k}}{\Delta r}, \tag{3.44}$$

$$L_z \equiv \frac{T_{i,j,k+1} - 2T_{i,j,k} + T_{i,j,k-1}}{\Delta z^2}. \tag{3.45}$$

According to what was described in Sect. 3.3, the basic time-stepping algorithm comprises a main loop repeating each time the following steps

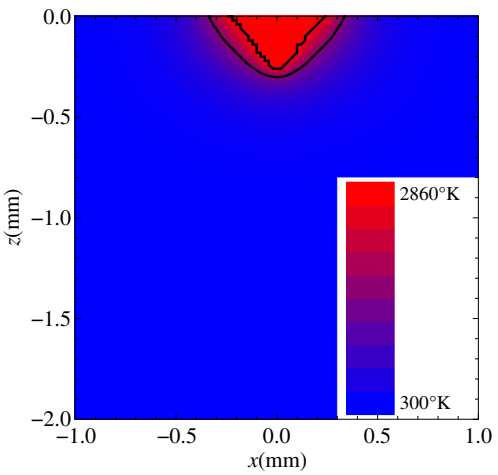

Fig. 4 The outcome of the model at t=3 msec

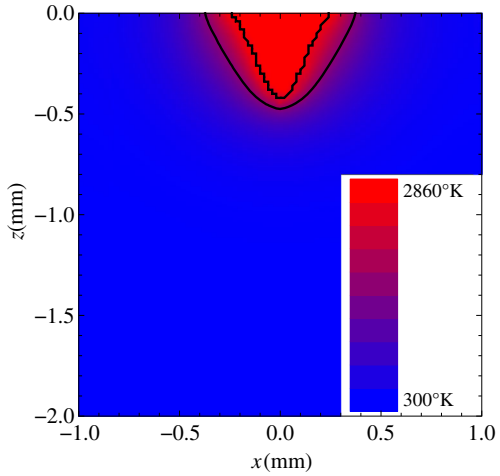

Fig. 5 The outcome of the model at t=6 msec

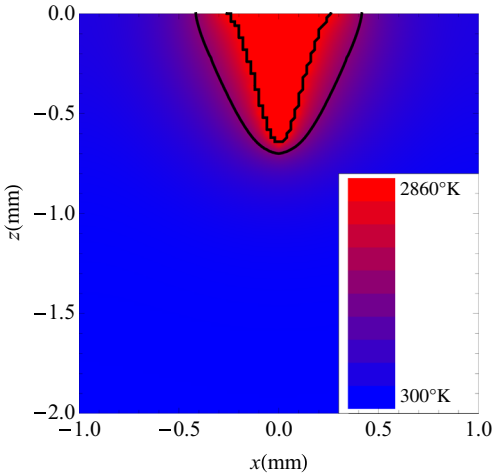

Fig. 7 The outcome of the model at t=12 msec

1. Calculation of the Laplacian of the temperature field at the time slice i. For this step, the keyhole shape has to be well specified, so as for the appropriate boundary conditions to be applied.
2. Calculation of the enthalpy density field and then of the temperature field at the time slice $i+1$, using the "enthalpy method."
3. Calculation of the shape of the keyhole from the enthalpy density field, so that it can be used in the next execution of the loop.

The above steps are depicted in Fig. 11.

The calculation of the radial part of the Laplacian is performed in every horizontal slice identified by k, from $j=br_{ik}$ to $j=N_r$. However, there are two possibilities for the boundary condition applied at $j=br_{ik}$. If br_{ik} is equal to 1, then the $j=br_{ik}$ element is not a physical boundary of the solid/liquid region. On the contrary, the work-piece extends up to the laser beam axis at r=0. In this case, there is only the singularity problem due to the polar coordinates that is resolved by Eq. (3.40). If br_{ik} is larger than 1, then the $j=br_{ik}$ element is a physical boundary of the system and the influx of energy from the laser beam has to be taken into consideration in the boundary condition, as described by Eq. (3.37). Then, all other elements of L_r can be directly calculated by Eq. (3.44), apart from the last one at $j=N_r$, which is given by Eq. (3.38). The flowchart of this calculation is depicted in Fig. 12.

The calculation of the vertical part of the Laplacian is performed along vertical slices identified by index j. The calculation is a little easier than that of L_r, since the $k=bz_{ij}$ element is always a physical boundary of the solid/liquid region. Thus, L_z can be calculated using Eq. (3.45), apart from the $k=bz_{ij}$ and k=N_z elements, which are given by Eqs. (3.35) and (3.36), respectively. The flowchart of this calculation is depicted in Fig. 13.

Once the elements of the Laplacian of the temperature field at the time slice i have been specified, the

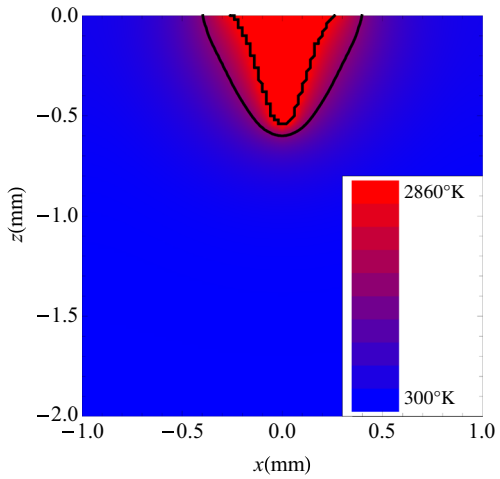

Fig. 6 The outcome of the model at t=9 msec

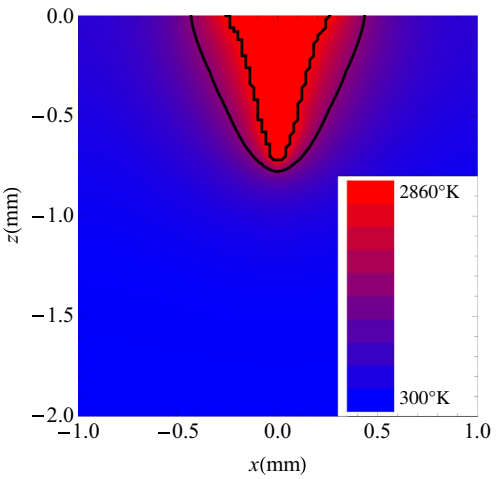

Fig. 8 The outcome of the model at t=15 msec

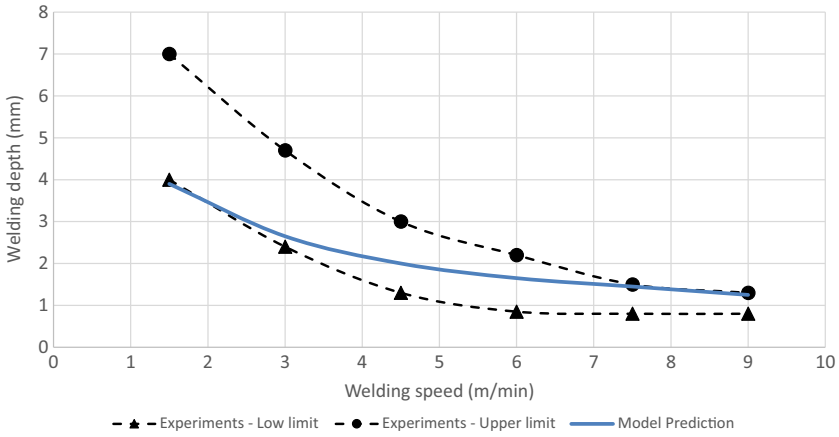

Fig. 9 Comparison of the model with experimental values [20]

Eqs. (3.19) and (3.20) can be used in order for the elements of the enthalpy density and temperature fields at time slice $i+1$ to be determined. The relevant flowchart is shown in Fig. 14.

Then, the specification of the boundaries has to be performed, so that in the next time slice, the appropriate boundary conditions can be applied. For the determination of the vertical boundary bz_{ij}, the formula (3.23) has to be applied. This formula reveals that the calculation has to be performed in vertical slices of the spatial lattice. Specifically, an element of the lattice is evaporated when the enthalpy density field is larger than the critical value for evaporation as it is specified by Eq. (3.18). Thus, starting from $k=N_z$, the algorithm has to compare the enthalpy density at the lattice elements with the critical value U_v. The first one that is found to exceed the critical value has vertical index k smaller by one than the wanted boundary of the time slice $i+1$. If the loop reaches $k=1$, without finding such an element, the loop has to end and the boundary should be set to 1. Special care has to be taken if the $k=N_z$ element is found to have evaporated. In this case, the entire vertical slice has evaporated, meaning that the user should have specified a lattice of larger depth for the particular

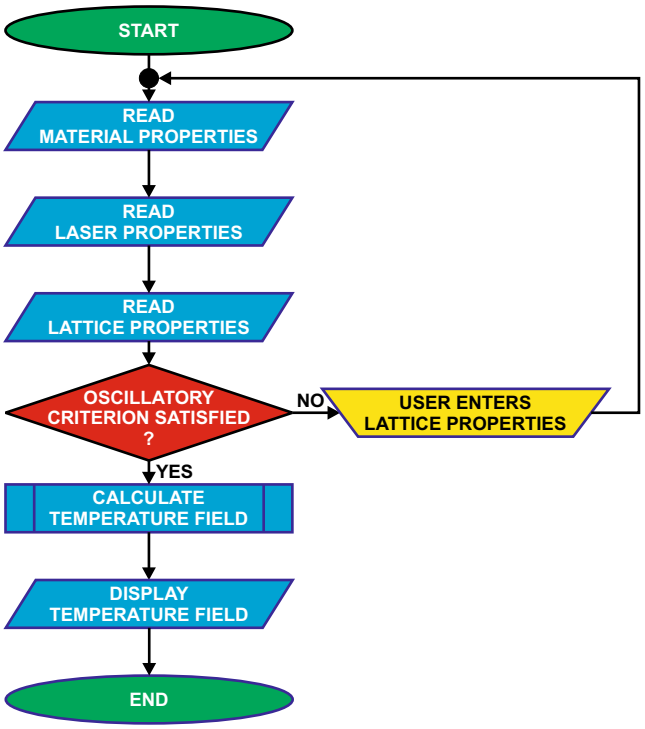

Fig. 10 Main implementation procedure

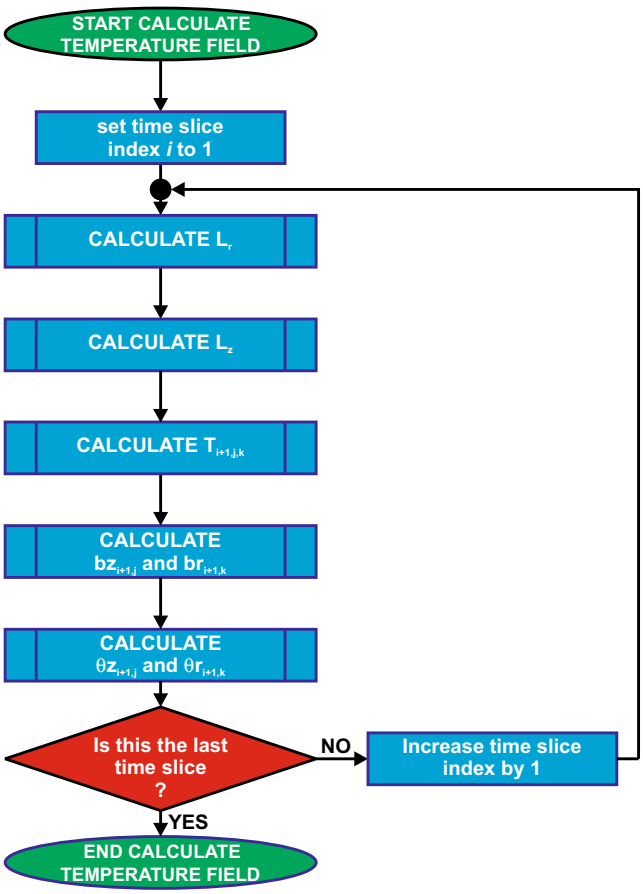

Fig. 11 The temperature field calculation subroutine

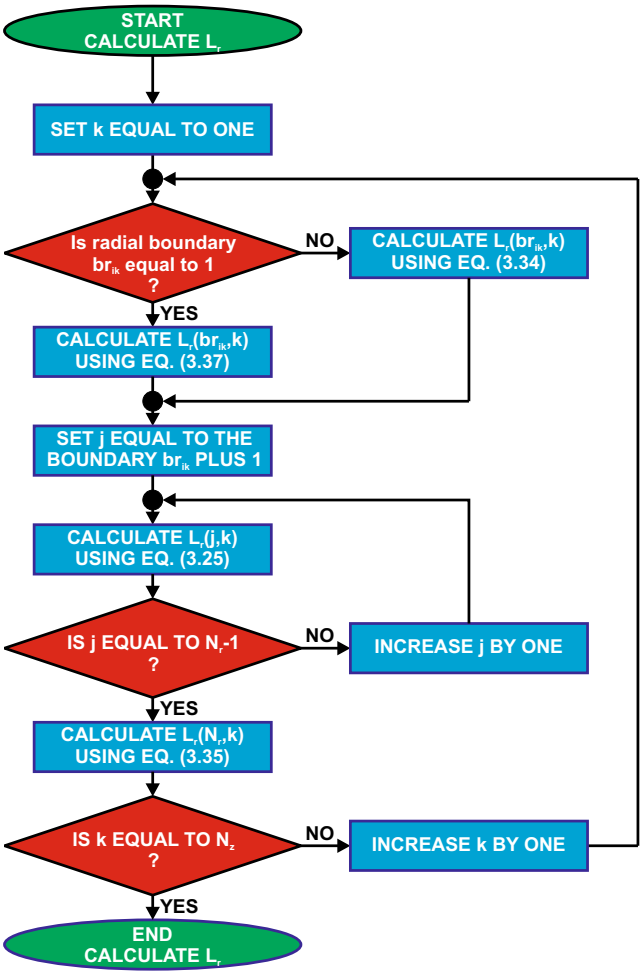

Fig. 12 The radial part of the Laplacian calculation subroutine

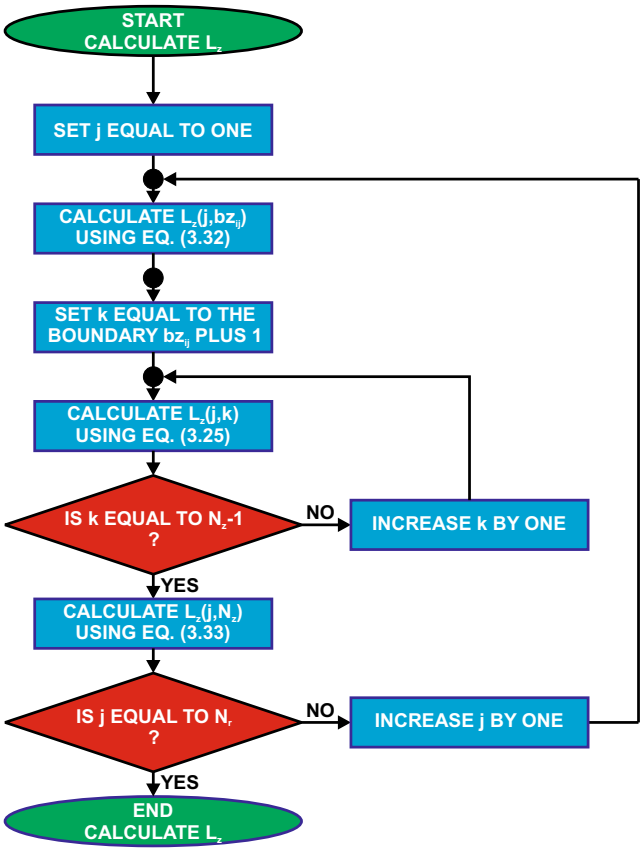

Fig. 13 The vertical part of the Laplacian calculation subroutine

process parameters; thus, an error message with this information should be displayed to the user, who has to specify new lattice properties for the problem. The workflow diagram for the specification of the vertical boundaries is shown in Fig. 15. The specification of the radial boundaries follows exactly the same flowchart, with the interchange of (j,k), (N_r,N_z), and (br,bz).

Finally, since the boundaries have been specified, the angles θr and θz can be easily calculated with the help of the Eqs. (3.25) to (3.30). Analytically, this calculation follows the flowchart of Fig. 16.

5 Discussion: a critical comparison with other methods

The existing methods (Sect. 2) mainly comprise simple analytical models [18, 29] or very elaborate numerical models, most of which are based on finite element techniques [16, 27, 28, 30].

In comparison to the analytical methods in the literature, the method presented has the following advantages:

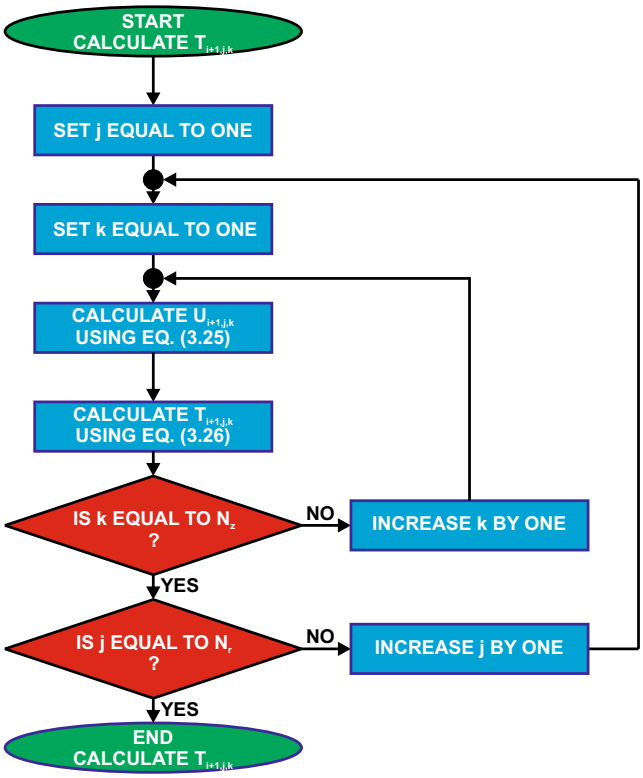

Fig. 14 The time-stepping calculation subroutine

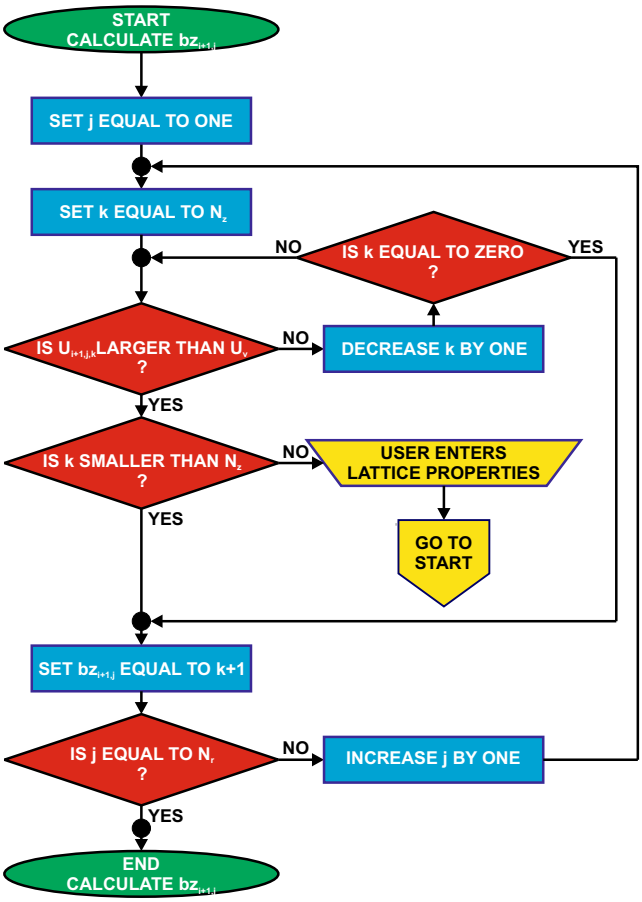

Fig. 15 The vertical boundary calculation subroutine

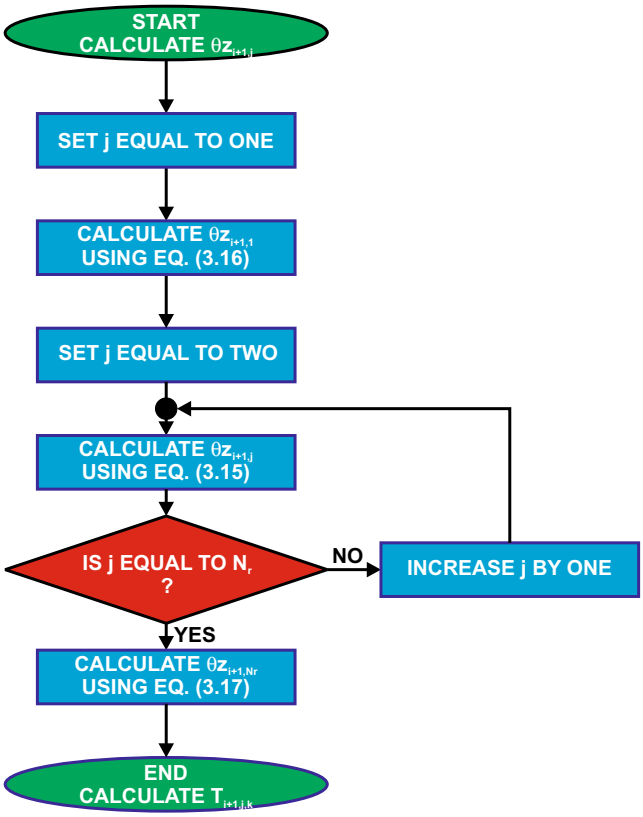

Fig. 16 The boundary angle calculation subroutine

1. It analyzes the thermodynamics of heating and phase transitions in great detail, providing high accuracy.
2. Most of the analytical models in the literature make some abstract assumptions about the geometry of the temperature field that are not accurate and cannot provide a good approximation for all process variables. On the contrary, in the method presented, no such assumptions are made.

Disadvantages:

1. Although the proposed algorithm runs quite fast, it is not as fast as the application of a simple formula as in the case of the analytical models. The running time cannot be as short as required for online monitoring and control. As might be expected, if an extensive running of the proposed model has been performed before the application, an empirical model based on the output, can be constructed and used for such applications.

In comparison to most of the numerical approaches, the proposed method has the following advantages:

1. The user has to specify only a few parameters to make the model running, namely the thermal properties of the material, some process variables related with the laser beam characteristics, and the parameters for the finite difference lattice. In a FEM, the user must specify the dynamics governing the thermal conduction, fine details about the lattice, and so on. Thus, the time for the preparation of a new material's simulation is significantly reduced.
2. The user does not have to take special care about the phase transitions. Using the enthalpy method, the proposed algorithm bypasses problems related with the fact that many phases coexist and interact during the keyhole laser welding.
3. The simplicity of the model enables the user to realize it in any computer language available and select the related advantage and disadvantages of his choice. The simplicity of the model renders the approach faster than any other finite element approach. Running time may be quite important if several runs of the models are necessary, for example, for the construction of an empirical model based on the model output.

Disadvantages:

1. Several finite element models can incorporate the fluid mechanics that describe the motion of the material in the liquid phase. Thus, it is expected

that these models may present a better accuracy for the process variables that correspond to high gas pressures.

2. The ready-made finite element software may have libraries, containing more detailed information about the thermal properties of the material used and their dependence on the temperature. However, such corrections can be easily incorporated into the proposed model.
3. Some ready-made finite element software allows the user to define a variable density of the elements lattice, this way enabling the user to focus more on the more interesting area. In the proposed approach, an equidistant lattice is used; however, this may also be altered at will.

6 Outlook

The numerical method presented in this paper deals with the multiple phase transitions taking place during laser welding. Further work will focus on loosening the simplifying assumptions, in order to include more physical phenomena, and furthermore on the experimental verification of the specific model and its future extensions, as well as on its appropriate adaptation to the experimental data.

Acknowledgment The work reported in this paper was supported by the collaborative program entitled "Remote Laser Welding System Navigator for Eco & Resilient Automotive Factories (RLW Navigator)," which is under the Seventh Framework Programme—FoF-ICT-2011.7.4: Digital factories: manufacturing design and product lifecycle management.

References

1. Li L, Hong M, Schmidt M, Zhong M, Malshe A, Huis in'tVeld B, Kovalenko V (2011) Laser nano-manufacturing—state of the art and challenges. CIRP Ann Manu Technol 60:735–755. doi:10.1016/j.cirp.2011.05.005
2. Tönshoff HK, Egger R, Klocke F (1996) Environmental and safety aspects of electrophysical and electrochemical processes. CIRP Ann Manuf Technol 45:2:553–568
3. Dahotre NB, Harimkar SP (2008) Laser fabrication and machining of materials. Springer, New York
4. De KJ, Duflou JR, Kruth J-P (2007) Monitoring of high-power CO2 laser cutting by means of an acoustic microphone and photodiodes. Int J Adv Manuf Technol 35:115–126
5. Chryssolouris G (1991) Laser machining: theory and practice. Springer, New York
6. Ready JF, Farson DF (2001) LIA handbook of laser materials processing. Magnolia Publishing, Inc., Laser Institute of America
7. Tsoukantas G, Stournaras A, Chryssolouris G (2008) Experimental investigation of remote welding with CO_2 and Nd: YAG laser-based systems. J Laser Appl 20:50–58
8. Klingbeil K (2006) What you need to know about remote laser welding: a look at how remote laser welding works and how it can be applied to your manufacturing process. Weld J 85:44–46
9. Zaeh MF, Munzert U, Oefele F (2007) Robot based remote laser-welding without scanner optics. In: Proceedings of the 4th International WLT-Conference on Lasers in Manufacturing, pp 1–8
10. Zaeh MF, Moesl J, Musiol J, Oefele F (2010) Material processing with remote technology-revolution or evolution? Phys Procedia 5: 19–33. doi:10.1016/j.phpro.2010.08.119
11. Fysikopoulos A, Anagnostakis D, Salonitis K, Chryssolouris G (2012) An empirical study of the energy consumption in automotive assembly. Procedia CIRP 3:477–482. doi:10.1016/j.procir.2012.07.082
12. Anthony P (2004) The reality of remote laser welding. In Laser Solutions 19:9–11
13. Bemenek M (2006) Technology report: welding from a distance. In Laser Solutions 21:19–23
14. Sabo DA (2007) The evolution of scanners for remote welding applications: the rise of beam quality leads to proliferation of remote welding applications. http://www.thefabricator.com/article/lasercutting/the-evolution-of-scanners-for-remote-welding-applications. Accessed on 15 May 2014
15. Verhaeghe G (2012) Remote laser welding for automotive seat production. In Laser Solutions 27:6–11
16. Abderrazak K, Salem WB, Mhiri H, Lepalec G, Autric M (2008) Modelling of CO_2 laser welding of magnesium alloys. Opt Laser Technol 40:581–588
17. Chen X, Wang HX (2001) A calculation model for the evaporation recoil pressure in laser material processing. J Phys D Appl Phys 34:2637–2642
18. Khan MMA, Romoli L, Dini G, Fiaschi M (2011) A simplified energy based model for laser welding of ferritic stainless steels in overlap configuration. CIRP Ann Manuf Technol 60:215–218
19. Phanikumar G, Chattopadhyay K (2000) Modeling of transport phenomena in laser welding of dissimilar metals. Int J Numer Methods Heat Fluid Flow 11:156–171
20. Kaplan A (1994) A model of deep penetration laser welding based on calculation of the keyhole profile. J Phys D Appl Phys 27:1805–1814
21. Ki H, Mohanty PS, Mazumder J (2002) Modeling of laser keyhole welding: part I. mathematical modeling, numerical methodology, role of recoil pressure, multiple reflections and free surface evolution. Metall Mater Trans A 33:1817–1830
22. Osher S, Sethian J (1988) Fronts propagating with curvature-dependent speed: algorithms based on Hamilton-Jacobi formulations. J Comput Phys 79:12–49
23. Burden RL, Faires JD (1993) Numerical analysis. PWS Publishing Co., Boston
24. Ki H, Mohanty PS, Mazumder J (2002) Modeling of laser keyhole welding: part II. simulation of keyhole evolution, velocity, temperature profile and experimental verification. Metal Mater Trans A 33: 1831–1842
25. Rońda J, Siwek A (2011) Modelling of laser welding process in the phase of keyhole formation. Arch Civil Mech Eng 11:739–752
26. Al-Kazzaz H, Medraj M, Cao X, Jahazi M (2008) Nd: YAG laser welding of aerospace grade ZE41A magnesium alloy: modeling and experimental investigations. Mater Chem Phys 109:61–76
27. Shanmugam NS, Buvanashekaran G, Sankaranarayanasamy K (2013) Some studies on temperature distribution modeling of laser butt welding of AISI 304 stainless steel sheets. World Acad Sci Eng Technol 7:1088–1097
28. Spina R, Tricarico L, Basile G, Sibillano T (2007) Thermo-mechanical modeling of laser welding of AA5083 sheets. J Mater Process Technol 191:215–219
29. Lampa C, Kaplan AFH, Powell J, Magnusson C (1997) An analytical thermodynamic model of laser welding. J Phys D Appl Phys 30: 1293–1299
30. Salonitis K, Stavropoulos P, Fysikopoulos A, Chryssolouris G (2013) CO_2 laser butt-welding of steel sandwich sheet composites. Int J Adv Manuf Technol 69:245–256. doi:10.1007/s00170-013-5025-7

31. Sugioka K, Meunier M, Piqué A (2010) Laser precision microfabrication. Springer Ser Mater Sci 135:91–120
32. Solana P, Negro G (1997) A study of the effect of multiple reflections on the shape of the keyhole in the laser processing of materials. J Phys D Appl Phys 30:3216–3222
33. Akhter R, Steen W, Cruciani D (1988) Laser welding of zinc coated steel. In: Proceedings of the 5th International Conference on Lasers in Manufacturing, pp 105–120
34. Mei L, Chen G, Jin X, Zhang Y, Wu Q (2009) Research on laser welding of high strength galvanized automobile steel sheets. Optics & Lasers in Eng 47:1117–1124
35. Bley H, Weyand L, Luft A (2007) An alternative approach for the cost-efficient laser welding of zinc coated sheet metal. CIRP Ann Manuf Technol 56:17–20. doi:10.1016/j.cirp.2007.05.006
36. Chen G, Mei L, Zhang M, Zhang Y, Wang Z (2013) Research on key influence factors of laser overlap welding of automobile body galvanized steel. Optics Laser Technol 45:726–733
37. Svelto O (1998) Principles of lasers. Springer, New York
38. Douglas J, Gallie TM (1955) On the numerical integration of a parabolic differential equation subject to a moving boundary condition. Duke Math J 22(4):557–571
39. Crank J (1987) Free and moving boundary problems. Oxford University Press, pp 424
40. Swaminathan CR, Voller VR (1993) On the enthalpy method. Int J Numer Methods Heat Fluid Flow 3:233–244
41. Patankar SV (1980) Numerical heat transfer and fluid flow. Hemisphere Publishing Co., Washington, New York, London, p 197
42. Voller VR, Cross M, Markatos NC (1987) An enthalpy method for convection/diffusion phase change. Int J Numer Methods Eng 24(1): 271–284
43. Morgan K (1981) A numerical analysis of freezing and melting with convection. Comput Methods Appl Mech Eng 28(3): 275–284
44. Morgan K, Taylor C, Brebbia CA (1980) Computer methods in fluids. Pentech Press, London, pp 257–284
45. Voller VR, Cross M (1981) Accurate solutions of moving boundary problems using the enthalpy method. Int J Heat Mass Transf 24(3): 545–556
46. Pastras G, Fysikopoulos A, Stavropoulos P, Chryssolouris G (2014) An approach to modeling evaporation pulsed laser drilling and its energy efficiency. Int J Adv Manuf Technol 72(9–12):1227–1241. doi:10.1007/s00170-014-5668-z